ORIGINAL ARTICLE

The effects of intensive aquaculture on nutrient residence time and transport in a coastal embayment

Bing Wang[1] · Ling Cao[2] · Fiorenza Micheli[3] · Rosamond L. Naylor[2] ·
Oliver B. Fringer[1]

Abstract Aquaculture in many countries around the world has become the biggest source of seafood for human consumption. While it alleviates the pressure on wild capture fisheries, the long-term impacts of large-scale, intensive aquaculture on natural coastal systems need to be better understood. In particular, aquaculture may alter habitat and exceed the carrying capacity of coastal marine ecosystems. In this paper, we develop a high-resolution numerical model for Sanggou Bay, one of the largest kelp and shellfish aquaculture sites in Northern China, to investigate the effects of aquaculture on nutrient transport and residence time in the bay. Drag from aquaculture is parameterized for surface infrastructure, kelp canopies, and bivalve cages. A model for dissolved inorganic nitrogen (DIN) includes transport, vertical turbulent mixing, sediment and bivalve sources, and a sink due to kelp uptake. Test cases show that, due to drag from the dense aquaculture and thus a reduction of horizontal transport, kelp production is limited because DIN from the Yellow Sea is consumed before reaching the interior of the kelp farms. Aquaculture drag also causes an increase in the nutrient residence time from an average of 5 to 10 days in the middle of Sanggou Bay, and from 25 to 40 days in the shallow inner bay. Low exchange rates and a lack of DIN uptake by kelp make these regions more susceptible to phytoplankton blooms due to high nutrient retention. The risk is further increased when DIN concentrations rise due to river inflows.

Keywords Aquaculture · Mariculture · Coastal embayment · Sanggou Bay · Kelp farming · Drag · Hydrodynamics · Numerical modeling · Nutrients · Transport

✉ Bing Wang
  bingwangice@gmail.com

1   The Bob and Norma Street Environmental Fluid Mechanics Laboratory, Stanford University, Stanford, CA 94305, USA

2   Center on Food Security and the Environment, Stanford University, Stanford, CA 94305, USA

3   Hopkins Marine Station and Center for Ocean Solutions, Stanford University, Pacific Grove, CA 93950, USA

🖉 Springer

1 Introduction

1.1 Aquaculture in China and previous studies

China's aquaculture industry, by far the world's largest, has over-taken capture fisheries and now accounts for more than 60% of the global aquaculture volume [7]. Its shellfish (molluscs and crustanceans) and seaweed production accounts for 70 and 50% of the global production, respectively [17]. China's mariculture (aquaculture in seawater) has grown ten-fold in the past two decades, mainly as a result of shellfish and seaweed farming in coastal regions [16]. In response to limited land and freshwater growth, mariculture is being promoted aggressively and further expansion is expected [7]. While such development in aquaculture provides great potential for alleviating pressure on wild capture fisheries [7], it also creates many environmental concerns, including the well-recognized problems of harmful algal blooms in China's coastal waters [50]. One of the greatest challenges is to understand the impacts of such intensive aquaculture and its underlying mechanisms, so as to balance the benefits and risks to ensure its long-term sustainability.

Since the 1980s, researchers have been studying how aquaculture modifies the flow field. Field observations have been carried out at different aquaculture sites around the world (e.g., see the work by [6, 13, 23, 26, 56]). Due to the complex interactions of aquaculture with the flow, sediment transport, and phytoplankton ecology, numerical models are useful tools to connect various facets of the problem to provide a more thorough understanding of how they are affected by aquaculture.

In this work, we chose Sanggou Bay as our study site, which is one of the largest aquaculture sites in China. Several models have been developed for Sanggou Bay. Grant and Bacher [24] developed a two-dimensional model, using Aquadyn 3.0 with roughly 200 nodes. It is among the first model studies on the frictional effects of suspended aquaculture, and they found that aquaculture led to a 20–50% reduction in current speeds in the bay. Duarte et al [11] developed a two-dimensional comprehensive model for Sangou Bay with roughly 1000 grid cells. It incorporates hydrodynamics, sediments, nutrients, aquaculture production, and phytoplankton-zooplankton dynamics, and successfully captured the seasonal variability of the system. Shi [44] developed a three-dimensional model for Sanggou Bay using POM [2] with roughly 800 grid cells to evaluate the carrying capacity for kelp production in the bay. An example of a related aquaculture system can be found in Kishi et al. [29], who developed a numerical model (roughly 1000 grid cells) to assist in the management of finfish cultivation in Mikame Bay, Japan.

Although the goal of numerical models is to answer questions related to economics, ecology, and management, accurate assessment of different scenarios relies on an accurate hydrodynamic core solver. With advances in computation in recent years, hydrodynamic solvers with much higher performance can be incorporated in aquaculture-related applications to provide better resolution and accuracy for in-depth analyses. A good example is the model recently developed by Wu et al. [49] using FVCOM [8] for fish farms in Fundy Bay, Canada. Their model has roughly 40,000 grid cells to cover the Gulf of Maine, while 15 cells are used to represent the aquaculture site. The model demonstrates good capability in predicting the near-field effects on currents and sediment erosion. In this manuscript, we develop a model of similar capability but to study the large-scale impacts of a considerably more extensive aquaculture site.

1.2 Background of Sanggou Bay

Sanggou Bay is a semi-enclosed bay located at the tip of the Shandong peninsula with the Yellow Sea to the east (Fig. 1). Due to the protruding geometry of the peninsula, the exchange between Sanggou Bay and the Yellow Sea is quite active. The bay has a surface area of 140 km^2 and an average depth of 8 m. Aquaculture occupies close to 90% of the water surface in the bay and now extends well outside the bay to where the water is 18–20 m deep [20]. Sanggou Bay has a long history of aquaculture, and a good amount of data has accumulated over the past two decades as summarized by Fang et al. [14]. The bay is generally considered to be a representative site for integrated multi-trophic aquaculture.

Aquaculture in Sanggou Bay consists primarily of suspended raft systems. The primary aquaculture species are kelp (*Laminaria japonica*), with a typical 70 kton annual yield, and bivalves (scallops and oysters), with a 60 kton annual yield. Kelp is attached to long ropes and bivalves are held in cages and nets [15]. Small quantities of finfish, abalone and sea cucumber are also cultivated [31]. Figure 2 shows the buoys on the water surface to demonstrate the scale and density of aquaculture in the bay. At such a large scale and high density, the growth of kelp and bivalves significantly alters the water chemistry and nutrient distribution in the bay [13]. Furthermore, aquaculture infrastructure and kelp blades add a considerable amount of drag and alter the flow structure in the horizontal and vertical [24, 44, 56]. As a result, nutrient transport, turbulence, sediment transport and other fundamental processes are all affected [56].

One of the primary concerns for aquaculture in Sanggou Bay is nutrient limitation. The average N/P (nitrogen to phosphorus) ratio in Sanggou Bay is around 4.1, significantly lower than the Redfield N/P ratio of roughly 16 required for marine algae growth [22]. Sanggou Bay is thus a nitrogen-limited system during most of the year [11, 45, 53]. The most severe DIN (dissolved inorganic Nitrogen) limitation occurs between March and June, which coincides with the peak kelp growth before its harvest. This has led to a reduction in quantity and quality of kelp production in the middle of the bay. Kelp death and decay begins as early as April, and up to 20% of the harvest does not meet quality standards for human consumption [55]. Transport from the Yellow Sea is the primary source of DIN in Sanggou Bay, which is to a great extent impeded by friction associated with aquaculture [44].
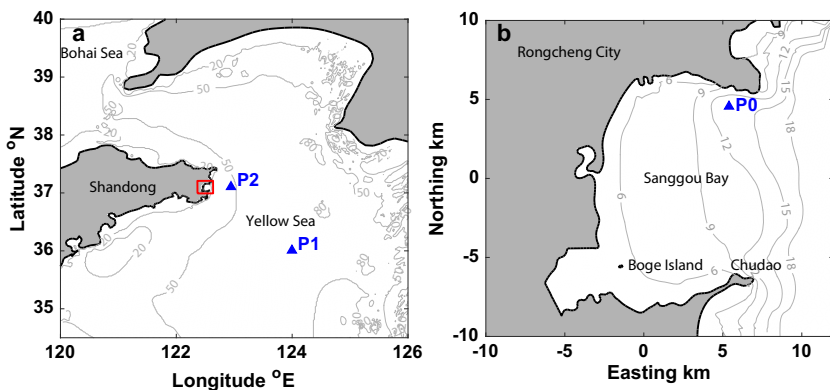

Fig. 1 Map of **a** the Yellow Sea and **b** Sanggou Bay. **b** Corresponds to the region within the red rectangle in **a**. Contours show the depth of the bathymetry. Locations P0, P1 and P2, indicated by triangles, are used for validation in Sect. 4. **b** Uses shifted UTM coordinates that will be explained in Sect. 2
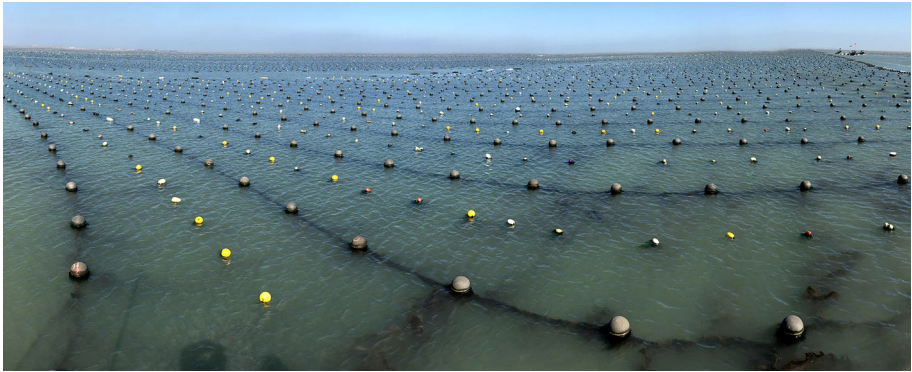
Fig. 2 Aquaculture buoys on the water surface in Sanggou Bay in 2016, looking south from the coast near location P0 in Fig. 1. Buoys on a rope are roughly 1–1.5 m apart

Another main concern in Sanggou Bay is the increased retention of nutrient and risk of harmful algal blooms in the shallow regions of the bay. The model study by Shi [44] suggested that the residence time in the southern region of Sanggou Bay is around 70 days, increased by 70% due to aquaculture (they defined their residence time as the time needed to dilute an instantaneous release of a substance to half its initial concentration), which is much longer than the time scale required for phytoplankton growth. As a result, this region has been deemed a high-risk zone for eutrophication and algal blooms [32]. In May 2011, a severe brown tide outbreak occurred in Sanggou Bay. Observations suggested that the outbreak originated in the inner-most regions of the bay and first spread to the southern regions. The brown tide lasted for months and led to large-scale kelp decay and bivalve death. Zhang et al. [52] pointed out that river input may have caused this outbreak because observed high nutrient levels coincided with low salinity regions. Because river inflows are small until mid-summer, they have not been investigated in previous model studies [11, 44]. For the first time, we examine the transport of river-input DIN and its interaction with aquaculture in the bay to provide a basis for assessing the risk associated with relatively small river inflows.

1.3 Goals and objectives

Several numerical models have been used as a quantitative tool to evaluate the effects of aquaculture in Sanggou Bay to assist with aquaculture planning [11, 24, 44]. All of these models set open boundaries at the bay opening, cutting through the kelp cultivation zone and treating the bay as a relatively isolated system. However, the protruding geometry of the Shandong peninsula and location of Sanggou Bay (Fig. 1) imply that the hydrodynamics in the bay are tightly coupled to the large-scale circulation in the Yellow Sea. Therefore, previous models failed to accurately capture the exchange between Sanggou Bay the Yellow Sea and how it is affected by aquaculture. To overcome this limitation and obtain more accurate results, our model implements a much larger domain, higher resolution, improved transport algorithms and a kelp drag function. The kelp cultivation regions in the model can be specified outside the bay and can readily be extended if more aquaculture is moved to deeper water outside the bay, as has been proposed for future development (China's 13th Five-Year Plan). Another advantage is that the model does not rely on local measurements for boundary forcing because the open boundaries are far from

the site of interest. The main drawback, as expected, is the high computational cost given that the model requires long run times on a parallel computer.

In this study, we present a three-dimensional numerical model of Sanggou Bay, with a domain size and resolution exceeding previous models of the bay. The goal is to examine the effects of intensive aquaculture on the residence time (defined as the time scale for a certain substance to remain in the bay) and nutrient transport in the bay through a set of numerical experiments. We focus on the physical aspects and simplify the biological component by restricting it to only a kelp growth module.

In the following sections, we first describe the setup, parameterization and validation of the numerical model. We then use the model to discuss:

1. the fundamental characteristics of the tidal flows and the spatial variability of residence time in Sanggou Bay in the presence of aquaculture;
2. the spatial distributions of DIN and kelp mass;
3. the impacts of aquaculutre induced drag on nutrient limitation and residence time distributions;
4. the transport of river-borne DIN and its interaction with aquaculture.

Although these questions are specific to Sanggou Bay, a similar approach can be applied to other aquaculture sites. We hope this work demonstrates that numerical modeling is an effective tool to assist with management and planning of coastal aquaculture for long-term sustainable development.

2 Model description

2.1 Governing equations

We use the SUNTANS model [19] to simulate the hydrodynamics in Sanggou Bay. The model solves the Reynolds-averaged Navier–Stokes equations with the Boussinesq approximation. Nonhydrostatic effects generally scale with the aspect ratio of the flow (the ratio of vertical sale to horizontal scale) and are insignificant in this case as the horizontal scale of the domain is much larger than the vertical scale. Due to the high computational cost of the nonhydrostatic pressure solver, we employ SUNTANS in its hydrostatic mode despite its nonhydrostatic capability. We employ a total variation diminishing scheme with the Superbee limiter for advection (implemented by Zhang [54]), and a higher-order interpolation method for cell-centered velocities (implemented by Wang et al. [47]). The governing equations for momentum are given by

$$\frac{\partial u}{\partial t} + \nabla \cdot (\mathbf{u}u) - fv = -\frac{1}{\rho_0}\frac{\partial p}{\partial x} + \nabla_H \cdot (v_H \nabla_H u) + \frac{\partial}{\partial z}\left(v_V \frac{\partial u}{\partial z}\right) + \sum \mathbf{F}_{D,x}, \qquad (1)$$

$$\frac{\partial v}{\partial t} + \nabla \cdot (\mathbf{u}v) + fu = -\frac{1}{\rho_0}\frac{\partial p}{\partial y} + \nabla_H \cdot (v_H \nabla_H v) + \frac{\partial}{\partial z}\left(v_V \frac{\partial v}{\partial z}\right) + \sum \mathbf{F}_{D,y}, \qquad (2)$$

subject to continuity

$$\nabla \cdot \mathbf{u} = 0, \qquad (3)$$

where $\mathbf{u} = (u, v, w)$ is the velocity vector with eastward, northward and vertical velocity components, respectively, $\sum \mathbf{F}_{D,x}$ and $\sum \mathbf{F}_{D,y}$ are the eastward and northward components

of the total drag forces, f is the Coriolis parameter, and p is the hydrostatic pressure. Under the hydrostatic assumption, there is no prognostic evolution equation for the vertical velocity w, which is solved from a vertical integration of the continuity equation (Eq. 3) instead. Due to the large size of the domain, we found it necessary to use a variable f linearized as a function of the latitude to obtain correct tidal propagation in the Yellow Sea. v_H and v_V are horizontal and vertical (turbulent) viscosities, and v_H is parameterized as a constant (see Table 1). v_V is computed with the MY2.5 turbulence closure scheme [3] in SUNTANS. Rosman et al. [42] showed that turbulent dynamics can be altered by the presence of kelp, causing distinct behavior in the turbulent kinetic energy and mixing length within the vicinity of the canopy. For simplicity, we neglect these effects on the large-scale circulation and transport because (1) the flow is dominated by a balance between pressure gradient and drag and (2) kelp occupies a small portion of the water depth. We make no modification on the turbulence closure for the reasons stated above, but when turbulence within the kelp layer is of particular interest, different closures may be necessary [28].

The governing equation for transport of a scalar Φ is given by

$$\frac{\partial \Phi}{\partial t} + \nabla \cdot (\mathbf{u}\Phi) = \nabla_H \cdot (\kappa_H \nabla_H \Phi) + \frac{\partial}{\partial z}\left(\kappa_V \frac{\partial \Phi}{\partial z}\right) + S_\Phi, \tag{4}$$

where Φ can be salinity, temperature or nutrients, and S_Φ includes the source and sink terms. For passive scalars like salinity, the source term $S_\Phi = 0$. For temperature, we calculate S_Φ using the thermodynamic model of Wood [48] implemented in SUNTANS by Rayson et al. [41], which includes the effects of shortwave radiation, incoming and emitted longwave radiation, and latent and sensible heat fluxes due to air-water temperature differences.

Table 1 Constants used in the momentum equations (Eqs. 1, 2), scalar and DIN transport equations (Eqs. 4 and 9) and kelp growth model (Eq. 10)

Parameter	Description	Value
v_H	Horizontal eddy-viscosity	1×10^{-2} m^2 s^{-1}
κ_H	Horizontal eddy-diffusivity	1×10^{-2} m^2 s^{-1}
z_0	Bottom roughness height	2.8×10^{-5} m
$C_{d,R}$	Drag coefficient of surface rafts	5×10^{-4}
S_d	Volumetric drag coefficient for kelp	1×10^{-3} m$^{1-\gamma}$ s$^{\gamma-2}$
$C_{d,BV}$	Volumetric drag coefficient for bivalve cages	1×10^{-3} m^{-1}
S_{SR}	DIN sediment release rate	4.8×10^{-3} μmol m^{-2} s^{-1}
S_{BV}	DIN bivalve excretion rate	1.08×10^{-2} μmol m^{-3} s^{-1}
R_{growth}	Maximum kelp growth rate	0.031 d^{-1}
R_{K2N}	Mass fraction of Nitrogen in kelp	1.4%
$R_{erosion}$	Kelp erosion rate	0.005% d^{-1}
k_{DIN}	Half saturation constant for DIN uptake	2.0 μmol L^{-1}
T_s	Optimal temperature for kelp growth	13 °C
T_e	Lethal temperature for kelp growth	25 °C
β_T	Constant in the temperature function	3.0

To represent the residence times in Sanggou Bay, we employ the mean age, as introduced by Delhez et al. [10] and Deleersnijder et al. [9]. To calculate mean age, we define the entrance of Sanggou Bay as the white line in Fig. 3b, which corresponds to the open boundary of previous models by Duarte et al. [11] and Shi [44]. When fluid enters the bay, it will have an 'age' represented by a scalar with an initial value of zero. It is then transported with the flow by Eq. 4 as it grows in time until exiting the bay. The mean age is thus the volume-averaged value of the age defined in each grid cell. If the fluid that leaves reenters the bay, its age will be reset to zero. Rayson et al. [41] describe the implementation of age in the SUNTANS model. Monson et al. [37] and Rayson et al. [41] showed that the mean age can be applied to study spatial heterogeneity and temporal variability of residence times in coastal systems. The method provides results similar to those produced by Lagrangian techniques but at a fraction of the computational cost because the evaluation of the Lagrangian residence times, defined as the time taken for a fluid particle at any location within the bay to leave the bay [4], requires calculation of trajectories of millions of particles. Therefore, we employ the mean age technique in this study.

2.2 Model domain and computational grid

The computational domain extends from Sanggou Bay to the Yellow Sea as shown in Fig. 3. The west ends of the bay near Lvdao Lake and Bahe Reservoir are bounded by dams. We use UTM coordinates (zone 51N) in the model and the origin is shifted to the center of Sanggou Bay. Bathymetry data combines a one minute dataset from GEBCO (General Bathymetric Chart of the Oceans) for the deeper regions and a finer dataset extracted from a regional seamap (China Navigation Chart No. 12110) for the region around Sanggou Bay. We employ an unstructured mesh with resolution varying from 200 m in the bay to 14 km near the boundaries (Fig. 3). The total number of horizontal cells is roughly 35k and there are 57 vertical layers in the z-level grid. The vertical resolution is 0.5 m for the top 30 m of the water column and stretched from one layer to the next by a factor of 1.1 below that. The bottom-most layer is 6 m thick and within the logarithmic layer of the bottom [34]. The minimum cell center distance is roughly 40 m and the time step size is 20 s as dictated by the horizontal momentum advection and propagation of internal gravity waves [19]. Computations are carried out on 24 processors, and it takes roughly 40 min of wall-clock time to compute 1 day of simulation.
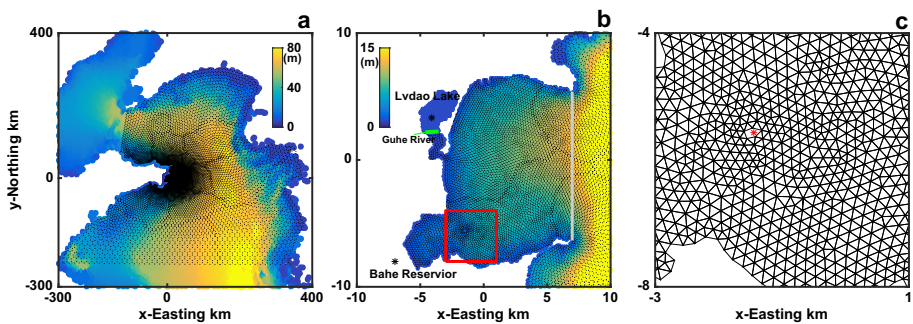

Fig. 3 Computational mesh and bathymetry employed in the model. The line across the bay opening in **b** defines the entrance of the bay for the calculation of mean age, and the green line is the open boundary for river inflow. **c** Shows the detailed mesh structure around Boge Island (indicated by the star) within the rectangle in **b**. Cell centers are shown in **a** and **b** for clarity, and cell edges are shown in **c**

The model has three open boundaries. Two are located in the Yellow Sea at the north and south ends of the domain. The free surface at these boundaries is forced by a linear superposition of the tides predicted by the TPXO tidal model (The OSU TOPEX/Poseidon Global Inverse Solution, 1/4 degree resolution, from http://volkov.oce.orst.edu/; Egbert et al. [12]) and the large-scale, low-frequency free-surface displacement from the global HYCOM model (1/12 degree resolution, from https://hycom.org; Bleck [1]). The third open boundary is for the river inflow, located at the west side of Sanggou Bay. Wind data (1 degree resolution) is derived from the Navy Operational Global Atmospheric Prediction System [43], consistent with the HYCOM model. Initial conditions for salinity and temperature are interpolated from the global HYCOM model.

2.3 Drag parameterization

Parameterizing drag is a key component of our model as it is implemented for the first time in SUNTANS for an aquaculture application. Due to the uncertainties associated with modeling drag in natural flows, we aim to estimate the drag coefficients at a representative order of magnitude. Various drag terms are accounted for, both as surface stresses and body forces. For most of them we follow the quadratic drag law, which is the drag on the flow per unit planform area of each grid cell,

$$\mathbf{F}_D = -\rho_0 C_d |\mathbf{u}| \mathbf{u}. \tag{5}$$

2.3.1 Bottom roughness

The bottom drag $F_{D,BT}$ is dictated by a roughness height parameter z_0. Assuming a log law, this drag coefficient is given by

$$C_{d,BT} = \left(\frac{ln(z_b/z_0)}{\kappa_{VK}} \right)^{-2}, \tag{6}$$

where z_b is the height of the bottom cell center above the bottom, and $\kappa_{VK} = 0.41$ is the von Karman constant. The roughness height in the Yellow Sea was estimated to be $z_0 = 2.8 \times 10^{-5}$ m by Liu and Wei [33] using measurements of dissipation in the bottom boundary layer. Inside the aquaculture zone in Sanggou Bay, Fan [13] estimated a roughness height varying between 0 and 1×10^{-3} m. As our model uses z levels, there is some inherent numerical drag owing to the stair-stepped nature of bottom slopes. However, such errors are small and comparable to the pressure gradient errors related to the alternative bottom-following grids such as sigma coordinates [36]. Given that numerical errors are unavoidable and there is also uncertainty in bathymetry, we do not vary the bottom roughness height and use a constant $z_0 = 2.8 \times 10^{-5}$ m for the entire domain for simplicity.

2.3.2 Infrastructure drag

The drag force due to the aquaculture infrastructure, $F_{D,R}$, is also accounted for. Rafts consist of floats and long ropes, and industrial standards dictate that the arrangement of the ropes should follow the main flow direction to reduce drag forces [35]. Zhang et al. [56] obtained field measurements in Heini Bay to the south of Sanggou Bay, and compared the velocities before and after the kelp harvest. They suggested that the drag from the rafts is

much smaller than that from the kelp and only causes a slight velocity reduction in the near-surface currents. Theoretically, the drag coefficient should change depending on the direction of the flow relative to the rafts. For simplicity, we use a constant $C_{d,R} = 5 \times 10^{-4}$ throughout the aquaculture zone in our model. This value is at the lower end of the estimates by Fan [13] and is calibrated using a qualitative comparison with the measured velocity profiles in Zhang et al. [56]. The drag force is applied in the top cell and calculated via Eq. 5 using the velocity in each grid cell.

2.3.3 Kelp drag

The drag force from kelp, $F_{D,K}$, is a body force applied in cells containing kelp. Kelp *laminaria japonica* is highly flexible and changes posture and shape as the flow increases [39]. As a result, the drag force increases more slowly than that indicated by the quadratic drag law in Eq. 5. Therefore, we follow the formulation for giant kelp *Macrocystis pyrifera* proposed by Gaylord et al. [21],

$$\mathbf{F}_{D,K} = -\rho_0 S_d |\mathbf{u}|^{\gamma-1} \mathbf{u}, \tag{7}$$

where $S_d = 0.5 A s_d$ is the effective drag coefficient determined by the total frontal area A and the empirical shape coefficient $s_d = 0.004$. The power $\gamma = 1.2$ is also empirically determined and is considerably lower than 2. Note that S_d is a dimensional number in units of $m^{1-\gamma}$ $s^{\gamma-2}$. For simplicity, we use local velocity u resolved by the grid in the kelp canopy as the reference velocity in the calculation, which is comparable to the depth-averaged velocity in this case. Gaylord et al. [21] showed that this formulation can reproduce the drag force even under rapidly changing wave conditions with currents of up to 0.4 m s^{-1}.

To determine the frontal area, we assume the width of the kelp blades is 0.1 m and add a factor of 0.5 to account for natural variation and twisting of the blades. The density of kelp is roughly 8–10 plants per unit area [44, 52], which gives $S_d = 1 \times 10^{-3}$ m$^{1-\gamma}$ s$^{\gamma-2}$ for the volumetric drag force. The drag force can be significantly reduced on an individual when placed within a canopy [5, 27, 38]. However, the empirical relation we use here from Gaylord et al. [21] is based on measurements over kelp patches in the field and hence accounts for the sheltering effect. The parameterization of Gaylord et al. [21] can reduce drag by roughly a factor of 50 in currents exceeding 0.2 m s^{-1} when compared to the quadratic drag law for a rigid cylinder of similar dimensions with no sheltering effects.

To implement the drag force with a smooth vertical transition, a linear decrease in kelp density is assumed within $\pm l_0$ of the mean kelp length l_{kelp}, where $l_0 = 1$ m. The body force per unit volume in the momentum equation is given by $\alpha F_{D,K}$, where

$$\alpha = \begin{cases} 1, & \text{when} \quad z > h - l_{kelp} + l_0, \\ \dfrac{z - (h - l_{kelp} + l_0)}{2 l_0}, & \text{when} \quad h - l_{kelp} - l_0 \leq z \leq h - l_{kelp} + l_0, \\ 0, & \text{when} \quad z < h - l_{kelp} - l_0, \end{cases} \tag{8}$$

and where h is the free-surface height and z is the height of a cell center.

Despite progress in past decades, modeling the resistance of vegetation in natural flows remains an open problem, due to the complexity of how the vegetation canopy interacts with the flow and turbulence [39]. The traditional method that treats individual plants as rigid cylinders can largely overestimate the total resistance from a canopy. The empirical formulation we adopt solves this problem. However, both methods require a reference

velocity that is difficult to define in unsteady flows (we use local cell-centered velocities). A recent porous media approach [58] that relies on geometric parameters can be a good alternative in applications with dense emergent vegetation in shallow flows [18, 25, 40, 57].

2.3.4 Bivalve drag

Drag from bivalve cages, $F_{D,BV}$, is also considered as a body force. In previous models of Sanggou Bay, this drag was treated in the same way as the kelp drag [11, 24] or not accounted for in the model [44]. Field studies have also not investigated their effects [13, 56]. Due to such a lack of data, we estimate a drag coefficient based on several theories to use with the quadratic drag law in Eq. 5.

According to Liu et al. [31], the cages for scallops are 0.3 m wide and 1.8 m long and are typically suspended at a depth of between 1 and 6 m below the surface. Cages are hung at horizontal intervals of 1 m along the rafts that are 5 m apart in the monoculture zone, and half of this density in the polyculture zone. To prevent an overestimate of the total drag, we conservatively assume that the effective drag force is 3% of that from an isolated solid cylinder of the same size, considering that: (1) the rafts are aligned with the main flow direction [35] and there can be significant sheltering effects [38]; (2) the cages have high porosity with fine net threads and the effective frontal area is likely a small fraction of the frontal area of solid cylindrical cages. We estimate the drag coefficient as $C_{d,BV} = 0.001$ m^{-1} in the monoculture zone, applied at a depth of 1–2.8 m below the surface. For oysters, although the cultivation methods are different, for simplicity we use the same value to represent both bivalve species. In the polyculture zone, because the cages are placed at lower density and sheltered by the kelp canopy, we assume they do not add additional drag to the flow.

Figure 4 illustrates the application of the drag terms described in this section in the different aquaculture zones. The outer bay consists primarily of a monoculture of kelp, the inner bay consists of a monoculture of bivalves, and the middle bay consists of a poly-culture zone for both species. Note that, to achieve similar reduction in velocity, the drag coefficients in our model are smaller than those used by Duarte et al. [11] and Shi [44]. The
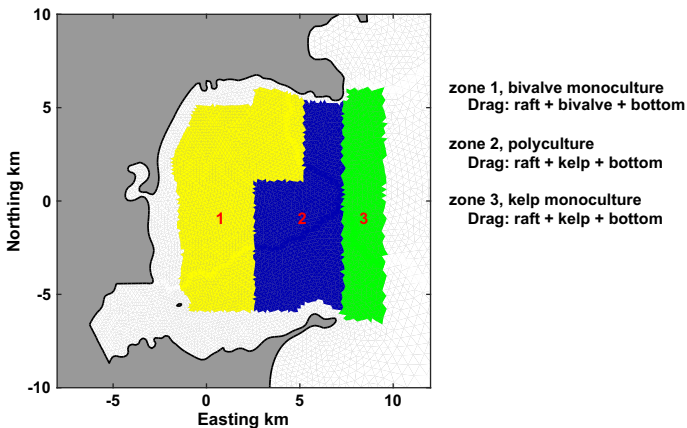

Fig. 4 Kelp and bivalve aquaculture zones to distinguish different drag parameterization and DIN sources in Sanggou Bay implemented in our model

lower drag in our model is expected given that when drag increases inside the bay, it reinforces the cross flow that passes the bay opening and reduces the flow entering the bay, an effect that was not captured in previous studies which employed smaller domains.

2.4 DIN sources

We summarize the sources and sinks of DIN during the peak season of kelp growth from March to May in Fig. 5, with estimates based on the data of Duarte et al. [11], Zhang et al. [55], and Shi [44].

The uptake by phytoplankton is estimated based on model results of Shi [44], and the transport term is estimated from the closure of the budget. All other terms are based on observational quantities. There are several seasonal rivers flowing into Sanggou Bay with an average annual runoff of 1.7–2.3 $\times 10^8$ m^3 and their DIN concentration can reach 300–600 umol L^{-1} [30]. However, due to low flow in spring, the measurements of Zhang et al. [51], Li et al. [30], and Li et al. [30] show no clear signal in salinity or DIN near the river outlets. Therefore, we do not include river input in the base case that is used for model validation, although we discuss the effects of different river flow rates in the test cases.

In the base case, we include sediment release and bivalve excretion as DIN sources, and the uptake by kelp as a sink. Transport is determined by the hydrodynamics from the model. We do not include the dynamics of particulate organic matter, phytoplankton and zooplankton due to limited data availability in the outer Yellow Sea. As shown in Fig. 5, even though the model does not include complex biological and grazing modules, it accounts for 70% of the total DIN balance. Note that the estimates in Fig. 5 are representative only of the peak growing season.

The model is run from March to May. For hydrodynamic forcing, we use the data from 2006, but for nutrients and kelp growth we use data from different years due to a lack of data at specific times. Therefore, the results are representative of a typical growing season rather than a specific year. For the DIN, we assume a uniform background concentration of 8 μmol L^{-1} in the Yellow Sea, based on various data sets that will be shown in the validation section. For the DIN distribution, the model is initialized with the result of a two month spin-up run and the average DIN concentration during the last 2 days is used. The new run reaches equilibrium in 3 days for velocity and DIN.

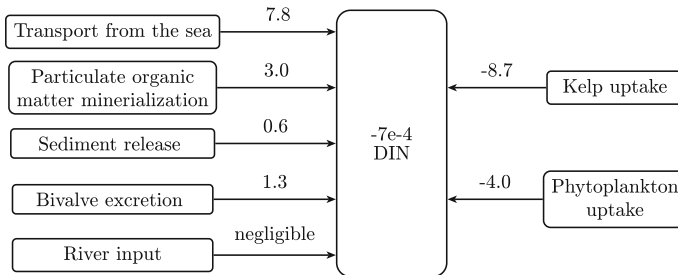The governing equation for DIN is similar to the scalar transport Eq. 4, and is given by

**Fig. 5** Average DIN release and uptake rates during the peak kelp growing season from March to May. Values are in ton d^{-1}

$$\frac{\partial\ DIN}{\partial t} + \nabla\cdot(\mathbf{u}\ DIN) = \nabla_H\cdot(\kappa_H\nabla_H\ DIN) + \frac{\partial}{\partial z}\left(\kappa_V\frac{\partial\ DIN}{\partial z}\right) + S_{DIN}, \qquad (9)$$

where $S_{DIN} = S_{SR} + S_{BV} - S_K$ is the total DIN source. S_{SR} is benthic sediment release, S_{BV} is bivalve excretion, and S_K is kelp uptake. Due to a long history of aquaculture, the sediment in the bay is composed of a thick layer of organic matter, forming a relatively steady source of nutrients to the water column. Therefore, the sediment release rate is assumed to be constant in space and time, and is given by a flux of DIN from the bed in the amount of $S_{SR} = 4.8\times 10^{-3}$ µmol m^{-2} s^{-1}, as estimated from 415.75 µmol m^{-2} d^{-1} from Shi [44]. Bivalves are an important source of DIN especially in the polyculture zone as their excretion is easily available to kelp. During the growing cycle from October to May, bivalves provide 278.46 ton DIN [44]. We assume a constant rate of $S_{BV} = 1.08\times 10^{-2}$ µmol m^{-3} s^{-1}, as a source of DIN at a depth of between 1.0 and 2.8 m beneath the free surface.

2.5 Kelp growth

For the calculation of kelp biomass, we use the dry weight unless otherwise noted. At the beginning of March (yearday 60), total kelp biomass is estimated to be 20 kton based on the results in Shi [44]. For simplicity, we assume the kelp density is spatially uniform. This is consistent with the fact that, during the winter season after the seedlings are planted in November, temperature and sunlight are the limiting factors for kelp growth and should lead to weak spatial variability at the scale of the bay. This gives an initial density of roughly 200 g m^{-2}. Zhang et al. [52] showed that the average length of kelp cultivated in Sanggou Bay is 1.9 m at the beginning of March and grows to 2.6 m in late May (around yearday 150). We fit a quadratic function to represent the relationship between length and time in their data as shown in Fig. 6. We assume a uniform distribution of kelp biomass with depth.

Fig. 6 Kelp length approximation based on the data in Zhang et al. [52]
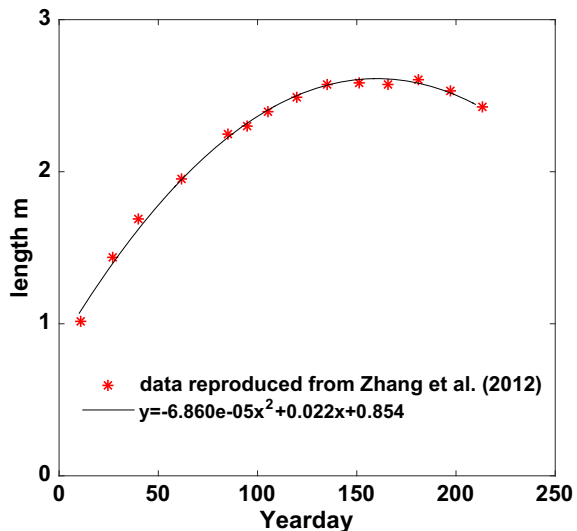
We follow the kelp model by Shi [44] (shown in their Equations 4-4 to 4-13) which includes a small erosion term but does not include the seedling and harvest terms in Duarte et al. [11] (shown in their Tables 2 and 3), which can be neglected for our simulation period. No kelp grazing by other organisms is included. The governing equation for kelp biomass per unit area, M_{kelp}, under DIN-limiting conditions is given by

$$\frac{dM_{kelp}}{dt} = \int_{h-l_{kelp}}^{h} \left(R_{growth} L_T L_{DIN} L_{light} - R_{erosion} \right) M_{kelp}/l_{kelp} \ dz, \tag{10}$$

where $R_{growth} = 0.031$ d^{-1} is the maximum net growth rate with L_T, L_{DIN} and L_{light} being the limitation functions due to temperature, DIN and light, respectively, and $R_{erosion} = 0.005\%$ is the kelp erosion rate. Integration is performed along the length of the kelp from depth $h - l_{kelp}$ to the free-surface h. Following Duarte et al. [11] and Shi [44], we assume $L_{light} \approx 1$ as sunlight is abundant during spring and the depth of the kelp can be adjusted slightly to maximize the growth rate. Kelp growth is computed as a vertical integral because we assume mass in kelp plants is distributed uniformly in the vertical. The corresponding DIN uptake rate by kelp per unit volume for use in Eq. 9 is then given by

$$S_K = R_{growth} L_T L_{DIN} R_{K2N} M_{kelp}/l_{kelp}, \tag{11}$$

where $R_{K2N} = 1.4\%$ is the mass fraction of Nitrogen in dry kelp. Limitation functions follow those used by Duarte et al. [11] and Shi [44]. Temperature limitation is given by

$$L_T = \frac{2.0(1.0 + \beta_T)X_T}{X_T^2 + 2.0\beta_T X_T + 1.0}, \tag{12}$$

where $\beta_T = 3.0$, and the temperature function $X_T = (T - T_s)/(T_s - T_e)$, where $T_s = 13$ °C and $T_e = 25$ °C are the optimal growth and lethal temperatures for kelp, respectively. The DIN limitation is $L_{DIN} = DIN/(DIN + k_{DIN})$, where $k_{DIN} = 2$ μmol L^{-1} is the half saturation constant for DIN uptake. Shi [44] performed a thorough sensitivity analysis on the kelp growth and DIN uptake model, which will not be repeated here. Recent work by Zhang et al. [53] provides a more dynamic kelp growth model that applies to the entire life cycle of kelp, which accounts for the elevated erosion rate and reduced net growth rate during the summer. Notation and the constants for the momentum equation, DIN transport, and kelp growth model are summarized in Table 1.

2.6 Base case and numerical experiments

In what we refer to as the base case (case B hereafter), parameterization for drag and DIN sources follows the descriptions above, and the results are used for validation in Sect. 3. To study the effects of aquaculture drag, a hypothetical scenario is studied in which the aquaculture layout is the same but is free of drag (case D0 hereafter). This is achieved by setting the drag to zero for kelp, bivalves and rafts, while the DIN sources and sinks associated with aquaculture are unchanged. The differences in mean age and DIN concentration between this case and the base case will be calculated and discussed.

To study how aquaculture interacts with river inflows, the following three scenarios are considered:

1. No aquaculture (case A0 hereafter), where aquaculture drag and DIN sources are set to zero and other conditions remain unchanged;
2. With aquaculture but no aquaculture drag (i.e. case D0 described above),

3. The base case (case B).

Reference model runs are first performed for the above scenarios with no river inflow, then experimental runs are performed with a hypothetic river inflow, and the differences in DIN concentration between the two sets of runs are used to illustrate the transport of river-borne DIN. Note that in case A0, the model gives a uniform DIN distribution because there are no sources and sinks.

Although multiple rivers drain into Sanggou Bay, we only consider the Guhe River which typically has the largest flow rate. The inflow is applied at the open boundary near the river inlet as shown in Fig. 3b. The mean annual discharge into the bay is 1.7–2.3×10^8 m^3, which gives a mean flow rate of 6 m^3 s^{-1}, and is much lower during the dry season [30]. The DIN concentration in the river can reach 300 μmol L^{-1}. In the model, we use a hypothetical flow rate of 1 m^3 s^{-1}, and a representative DIN concentration of 100 μmol L^{-1} for the river inflow.

All simulations were performed for the peak kelp growing period from March to May of 2006. River inflow is added during the first neap tide on March 10, 2006, after the tidal flows reach equilibrium. We neglect the density effects of the river inflow and set its salinity equal to that in the boundary cell, because even during the high-flow season there is just a 1–2 psu difference in salinity near the river inlet [30]. It is likely that the salinity gradient is located upstream and is sufficiently mixed by the time it reaches the river mouth.

3 Model validation

3.1 Off-shore tides

Predictions of tides in the Yellow Sea are validated at location P1 and P2 (see locations in Fig. 1) at depths of 80 and 40 m, respectively. Location P1, which is one of the TPXO validation points [46], is representative of large-scale variability of the Yellow Sea, and location P2 is representative of the tidal elevations close to Sanggou Bay. Although actual measurements are not available, the TPXO prediction accurately represents the free-surface elevation in the Yellow Sea, especially in the deeper regions [46]. As shown in Fig. 7,
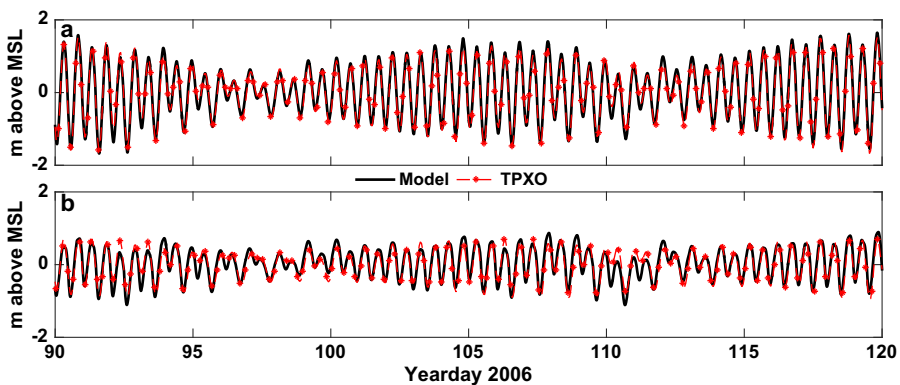

Fig. 7 Comparison of the free-surface predictions from the model to the TPXO model at location **a** P1 and **b** P2

our model captures the free-surface variation very well at both locations, both in amplitude and phase. At location P2, however, errors are slightly greater, mostly as underpredictions of high tides. Location P2 is shallower and closer to the coast where the slopes are relatively steep. The model predictions show nonlinear effects, while the TPXO predictions remain sinusoidal. It is likely that, because the TPXO model employs a resolution of 1/4 degree (roughly 25 km), it does not resolve the coastline or the bottom slope at location P2 and so we do not expect accurate TPXO predictions at this location. We also note that, although wind forcing is accounted for in our model, the free surface variation in the Yellow Sea is predominantly driven by the tides during the simulated period.

3.2 Free surface and currents in the bay

Predictions of free surface and currents in Sanggou Bay are validated at location P0 where observational data are published in Shi [44] and Fan [13]. The data in these two sources were from the same field observation in 2006, and we reproduce the data from their published figures. As shown in Fig. 8, at location P0, a station at the northern end of Sanggou Bay, the model captures (1) the correct amplitude and phasing, (2) the spring-neap variation, (3) the variation of high-high and low-high tidal amplitude within 1 day caused by the semi-diurnal M2 tidal constituent, and (4) a 0.8 m-drop in free surface due to a strong wind event around yearday 110 (April 20). The amplitude and phase are overall in good agreement with the observations, and the biggest deviations occur when the model underpredicts low water during the neap tide.

Depth-averaged currents from our model are validated at location P0 as shown in Fig. 9. Observational data is reproduced from Shi [44]. During the flood tide when the free surface rises in the bay, the flow is primarily westward at the northern opening and eastward at the southern opening. The currents offshore outside the bay are southward. Therefore, the west-east component, u, is dominant at location P0 and $u < 0$ during flood tide controlling the transport into the bay. The model prediction of u is in good agreement with the observations and captures the spring-neap variability (Fig. 9a). The largest errors occur in the peak eastward ($u > 0$) currents during spring tide with an underprediction of 10–25%. At a more detailed scale, Fig. 10a shows that the predicted u has wide, blunt peaks. It is important to note that the observed currents are more sinusoidal because they have been low-pass filtered to retain only six major tidal constituents [13, 44]. When tides encounter shallow water and interact with irregular coastlines, they deviate from a sinusoidal shape, as demonstrated by measurements from year 1999–2000 in Duarte et al. [11] (their Fig. 7). Therefore, we do not expect the observations at location P0 to retain the high-frequency signals due to the complex headland flows in the discussion below.
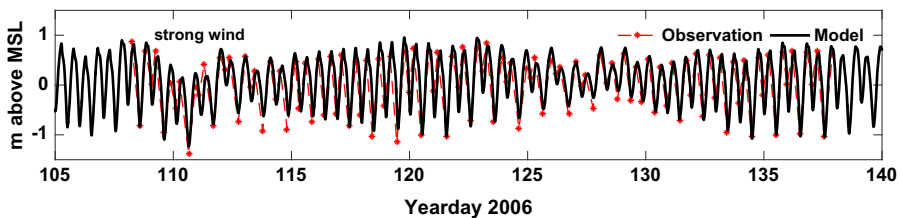

Fig. 8 Comparison of the free-surface predictions from the model to observations from Fan [13] at location P0
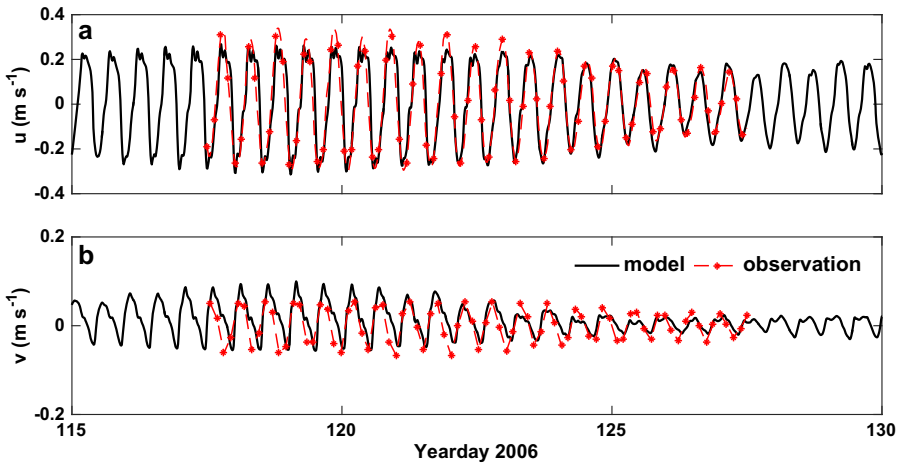
Fig. 9 Comparison of the predicted and observed depth-averaged **a** easting and **b** northing velocities at location P0. Observational data is reproduced from Shi [44]
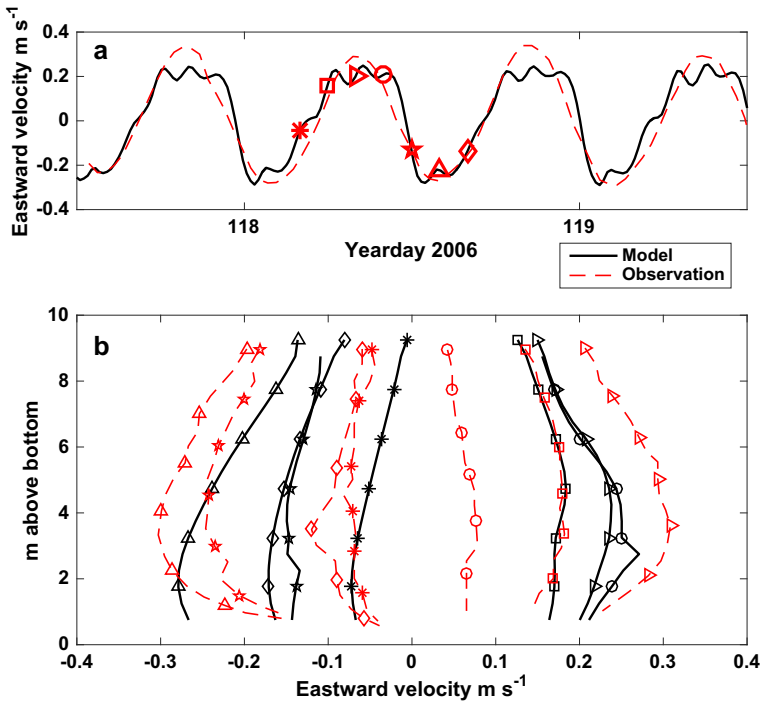

Fig. 10 Comparison of predicted and observed velocity profiles at location P0. **a** Depth-averaged velocities, **b** predictions and observations of *u* profiles from the model at 2-h intervals. Observational data is reproduced from Shi [44]. Markers in **b** correspond to the time steps shown in **a**

The south-north current, v, is considerably smaller, with a maximum of 0.07 m s^{-1} during the spring tide. Fig. 9b shows that the model underpredicts the amplitude of the flow especially in the southward direction (negative values). The shoreline near P0 is a headland with strong curvature and concavity (Fig. 1), and recirculation is predicted by the model during the flood tide at this location, while separation is predicted during the ebb tide on the north side of the headland. Oscillations in the velocity shown in Fig. 9a, b are caused by this recirculation and separation at different stages of the tide. For example, recirculation forms shortly after the flow reaches peak flood ($u < 0$), and during the slack tide when the flow reverses direction. Strong separation and recirculation occurs on the north side of the headland during peak ebb ($u > 0$). These features coincide with the oscillations in the velocity signal and only occur when the currents are strong during the spring tide. Accurate reproduction of these flow features requires high grid resolution and accurate bathymetry and aquaculture data, and the model may overpredict their strength because we do not include aquaculture in neighboring bays due to a lack of observations.

As shown in Fig. 10b, c, the predicted velocity profiles capture the most important features of the observations. The maximum velocity occurs in the middle of the water column at 6–7 m depth. Strong velocity gradients occur near the free surface due to the friction from the aquaculture. Furthermore, the velocity profiles are close to symmetric in time for flood ($u < 0$) and ebb ($u > 0$) tides. The profile denoted with circles is the only one that is significantly out of phase with the measurements, and it is caused by an extended peak ebb tide in the model as a result of strong nonlinearity.

In summary, the model has been developed through the use of publicly available data resources and yet showed strong predictive capability for the tidal flows in Sanggou Bay. Validation is carried out for both the tides in the Yellow Sea and the free-surface and currents in Sanggou Bay using TPXO results and observational data published by Fan [13] and Shi [44]. While a major advantage of the model is that it has been developed and validated based on publicly available data, some of the data may be inaccurate, further contributing to model uncertainty. In particular, lack of accurate bathymetry data or knowledge of the precise layout of aquaculture in 2006 leaves room for future improvement. Validation data can also be improved and unfiltered raw data is needed, particularly for validation of high-frequency motions. Finally, measurements at an offshore location outside the kelp cultivation zone should help improve the validation of offshore forcing.

3.3 Temperature and salinity

For temperature validation, Fig. 11 shows the model results of temperature at location P0 and a location in the middle of the bivalve zone along the inner bay. Overall, the temperature predictions are well within the range of observations from various sources (measured at different locations throughout the bay). The thermodynamic model of Wood [48] has captured the seasonal temperature increase from 4 to 14 °C during the simulation period. Toward the end of the simulation, the temperature is close to the optimal temperature for kelp growth, a well-known feature of Sanggou Bay [44].

At the end of the simulation, the model predicts a smooth east-to-west horizontal temperature gradient varying from 10 °C at the bay opening to 13 °C in the bivalve zone in the inner bay, which is consistent with the pattern observed by Zhang et al. [52] in 2011. The predictions at the two location shown in Fig. 11 highlight this gradient. In the vertical, the model predicts a temperature difference of up to 2 °C in the mid bay in the polyculture zone beginning from late April (around yearday 110, results not shown), which increases
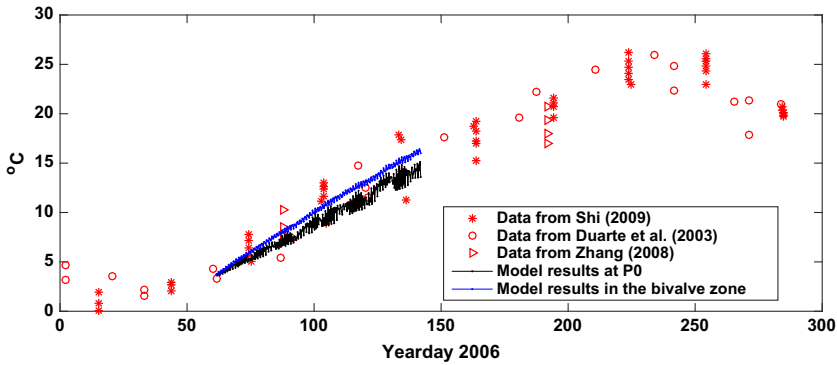
Fig. 11 Comparison of temperature predictions at location P0 and in the bivalve zone to observations from multiple sources. Predictions of temperature in the top layer at location P0 and a location in the middle of the bivalve zone are shown. For clarity, model results are plotted every 5 h

the stratification strength of the water column. However, the influence of stratification on horizontal transport is secondary compared to that of the aquaculture drag, and we do not include it in this study.

Salinity variation is minimal in the bay during the simulation period due to negligible river inflow. Measurements by Zhang et al. [51] show that at the end of April, the salinity is nearly uniform in space, ranging from 31.3 to 31.7 psu across the bay and thus salinity-induced stratification is negligible. In our model, the salinity varies from 31.5 to 31.6 psu across the bay after initializing with HYCOM, and does not change considerably over time, which is consistent with observations. Unlike temperature, salinity has a weak effect on most biological processes and does not impact kelp growth. Therefore, during the simulation period, salinity plays a weak role in both hydrodynamics and biology.

Fig. 12 Comparison of the DIN predictions to multiple observational datasets. Predictions are from the top layer at location P0, kelp zone (near the bay opening) and bivalve zone in the inner bay. Model results are shown at every 30 h for clarity
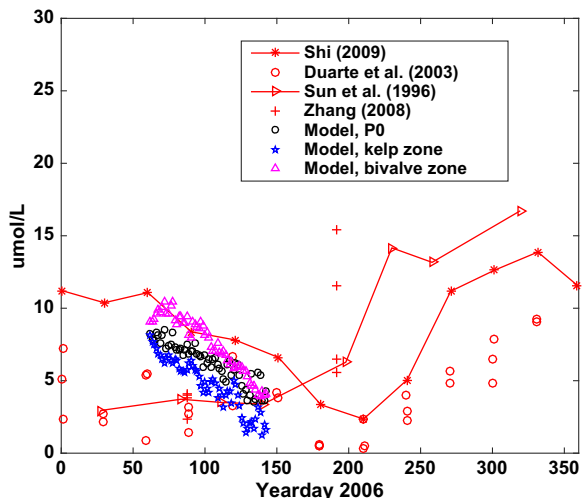
3.4 DIN concentration

In Fig. 12, we validate model predictions of DIN concentration at several locations using multiple datasets. Due to the spatial variability of DIN in the bay and its sensitivity to aquaculture, there is considerable variation between different datasets or even within the same dataset. However, the decrease in DIN during spring-summer seasons is apparent in the data. This decrease is caused by the growth of kelp and phytoplankton as discussed by Sun et al. [45] and others. The model captures this decreasing trend in DIN over the simulation period, with values and slopes aligned well with the range of those in the observations. Despite the overall decreasing trend, strong spring tides can cause short-term increases in DIN concentration in the kelp zone due to more effective transport from the Yellow Sea to the bay. Results also show that the DIN concentration in the bivalve zone is persistently higher than that in kelp zone at the bay opening over the simulation period.

In Fig. 13, we validate the horizontal DIN distribution in the bay. At the end of April (around yearday 120), the model predicts low DIN concentrations of 1μmol L^{-1} in the southern end of the kelp polyculture zone as shown in Fig. 13b, indicating significant nutrient limitation. The spatial variability is qualitatively in good agreement with the observations shown in Fig. 13a.

The model gives a reasonable prediction of kelp production, which relies on correct predictions of DIN concentrations in the bay. At the end of the simulation, the total kelp biomass predicted by the model is 76 kton, close to the reported production of 85 kton in 2007 [31], and slightly higher than the predicted 65 kton by Shi [44] for May 2006.

4 Results of the base case

4.1 Velocity field

The general pattern of the predicted tidal flows is consistent with previous work on Sanggou Bay, but strong gradients and local-scale recirculations are revealed by the high resolution of our model. Figure 14 illustrates the predicted surface velocity field during flood and ebb tides. During the flood tide, currents flow from north to south into the bay, and vice versa during the ebb tide. Overall, the currents in the bay are considerably weaker
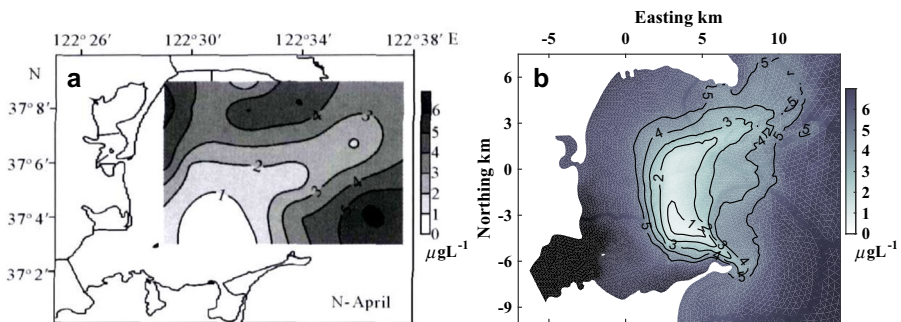

Fig. 13 Comparison of the DIN distribution predicted by the model to observations. **a** Is the observational data for April 2006 from Zhang et al. [52] (a direct copy of their Fig. 5A, with permission) and **b** is the model prediction at low tide on April 30
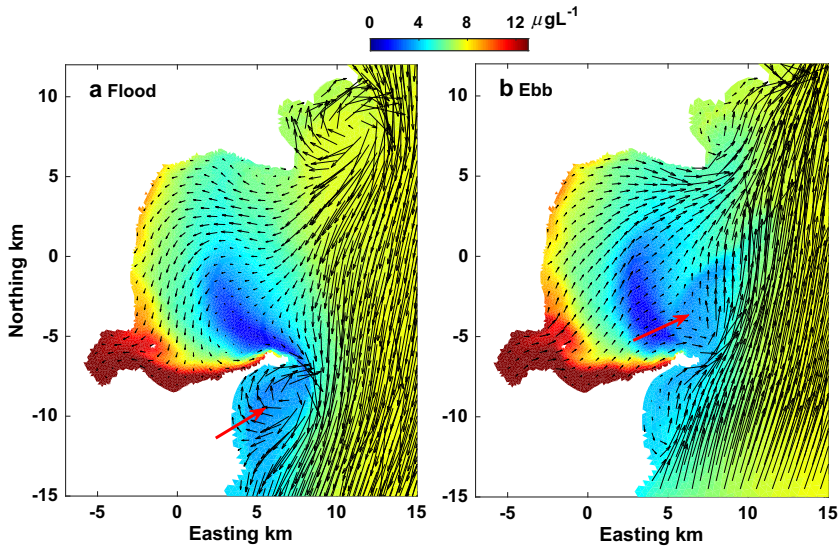
Fig. 14 Model results of surface velocity during **a** flood tide and **b** ebb tide on April 30, 2006. Background color shows DIN concentration. The red arrow indicates the location of recirculating eddies discussed in the text

than the offshore cross-flow, especially in the southern part of the bay. The northern region is flushed more than the southern region both during flood and ebb tides. At the mouth of the bay, a clear deceleration of currents occurs and coincides with the outer edge of the kelp monoculture zone. Chudao Island (the headland at the southern opening of the bay) consistently causes recirculation in its wake, which also occurs at other similar locations along the coastline.
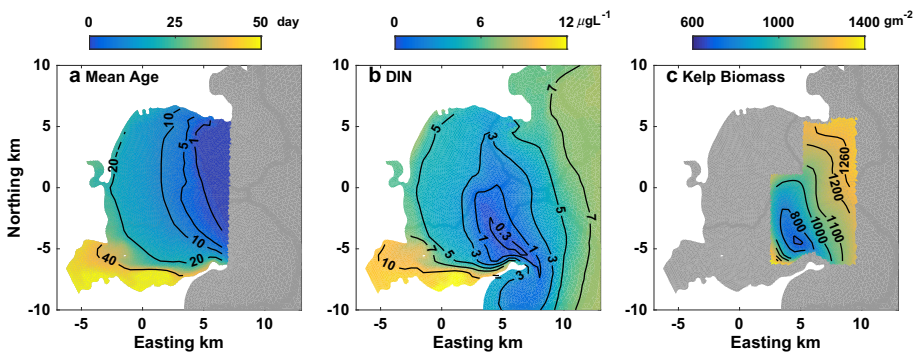

Fig. 15 Model results of surface **a** mean age, **b** DIN concentration, and **c** kelp mass distributions on May 20, 2006. The gray region in **a** is outside Sanggou Bay where mean age is not defined, and the gray region in **c** is outside the kelp zone where no kelp is cultivated. Color schemes and contours show the same data in each plot

4.2 Mean age, DIN and kelp mass distribution

As shown in Fig. 15a, under the aquaculture layout shown in Fig. 4, the majority of the bay has a mean age (defined in Sect. 2) of less than 25 days, while the southern inner bay and the southwestern corner (around Bahe Gang) has the longest mean age that exceeds 50 days. This distribution is consistent with the distribution of "half exchange time" in Shi [44], although the values are not equal due to different definitions of the mean age and "half exchange time".

For DIN distribution (Fig. 15b), the model predicts strong horizontal variability. Overall, the tidal flow flushes the bay and transports nutrients from north to south, leading to a lower DIN concentration at the southern opening. In addition to the large zone of low DIN in the southern region of the bay, a smaller low DIN region is formed due to trapping by an eddy that is shed from Chudao Island during the flood tide (red arrow in Fig. 14a). This low DIN region is transported north by the subsequent ebb tide (red arrow in Fig. 14b), demonstrating how eddies can alter the DIN distribution in the bay, an effect not captured by previous models. Most of the aquaculture region has a DIN concentration of less than 5 μmol L^{-1} and the lowest is less than 1 μmol L^{-1} in the middle of the bay in the kelp polyculture zone, as shown in Fig. 15b (also Figs. 13b and 14). When the DIN concentration is lower than 1 μmol L^{-1}, kelp growth is hindered and native benthic vegetation may be eliminated. In the inner bay, the DIN concentration is high as shown in Fig. 15b due to persistent sources of DIN from benthic sediment and bivalves. These regions are thus more susceptible to phytoplankton blooms.

The distribution of kelp biomass in Fig. 15c also shows strong gradients within the bay. Even though the competition of phytoplankton is not accounted for in the model, the yield of kelp can be as low as 600 g m^{-2} due to DIN limitation alone. The results strongly suggest that the kelp density inside the bay, especially in the south, should be reduced to alleviate nutrient limitation and improve kelp quality. Note that the kelp farms in neighboring bays along the coast of Shangdong Peninsula certainly affect Sanggou Bay, although this is not accounted for in the model.

5 Numerical experiments

5.1 Impacts of aquaculture drag on transport

To evaluate the effects of aquaculture drag, hypothetical test case (D0) is performed by assuming no aquaculture drag and compared with the base case (B) (details of the setup are described in Sect. 2.6). All results are from the surface layer at the end of the simulation, during the flood tide on May 20, 2006.

Overall, model results indicate that the intensive aquaculture considerably reduces currents and increases the mean age in Sanggou Bay. As shown in Fig. 16a, b, there are considerable differences in velocities between case D0 and B in the kelp zone, in terms of both magnitude (shown with color) and direction (shown with vectors). The greatest difference is in the kelp monoculture zone near the opening of the bay, where the currents are more than 30% larger in case D0. In the bivalve monoculture zone, the difference is smaller.

Figure 16c, d illustrate the mean age distribution in case D0 and the differences from case B. In the mid and inner bay, in the absence of aquaculture drag, mean age is reduced
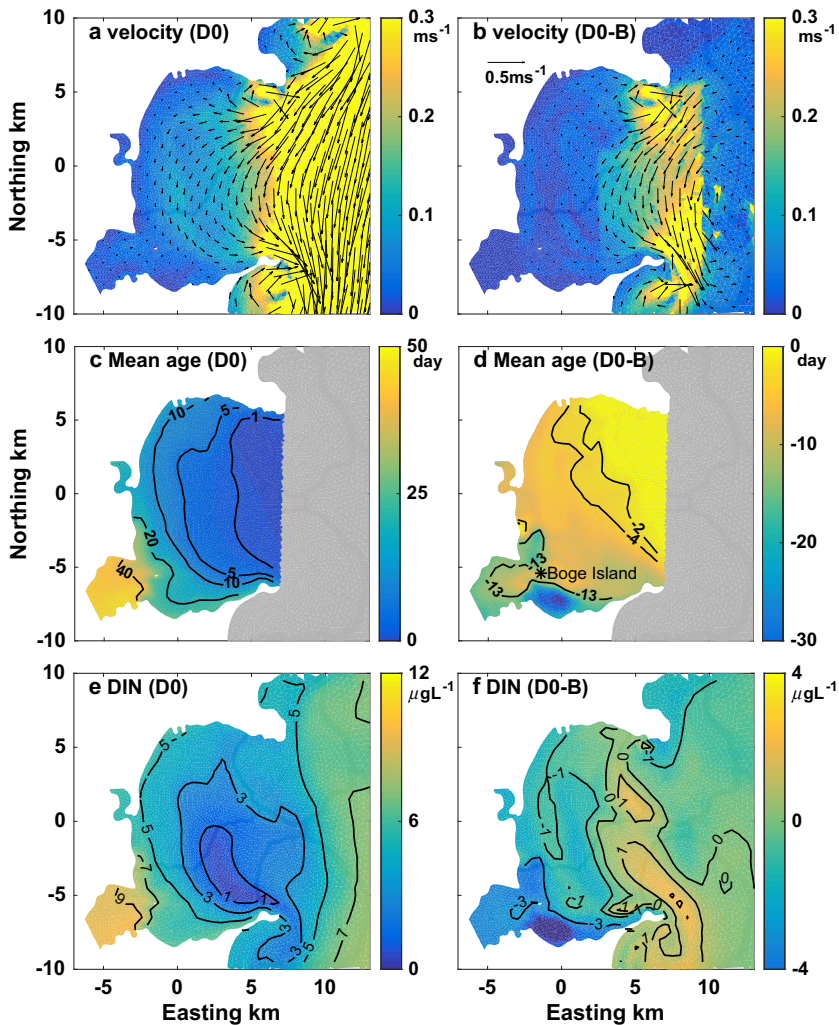
Fig. 16 Model results of the test case with no aquaculture drag (case D0) and differences from the base case (case B): **a** velocity, **b** difference in velocity (D0-B), **c** mean age, **d** difference in mean age (D0-B), **e** DIN concentration, and **f** difference in DIN concentration (D0-B). In **a** and **b**, color shows the magnitude of velocity vectors. Color schemes and contours show the same data in each plot. All results are from the surface layer at the end of the simulation on May 20, 2006. The location of Boge Island is shown with a star in panel (**d**)

by 4–8 days in a relatively uniform fashion, which is a 30–70% reduction compared to case B. Differences are more prominent along the east-west and north-south directions with differences of 13–17 days around the poorly-flushed southwestern corner and around Boge Island. To the south of Boge Island, the model predicts a reduction of 30 days in the mean age in case D0, the most significant in the entire bay. This location has slightly deeper bathymetry and a different type of bottom sediment from neighboring locations as shown on navigation charts (China Navigation Chart No.12110). It is suggested to be possibly

occupied by rocks and a small number of fish cages [32] that are not resolved in the model. Therefore, the model may be missing certain local dynamics at this site.

By reducing currents and transport, aquaculture drag contributes both to the DIN limitation in the kelp zone and the retention in the southwestern corner of the bay. As shown in Fig. 16e, f, in case D0, the lowest DIN concentration, which occurs in kelp-bivalve polyculture zone, increases by 1–2 μmol L^{-1} compared to case B. In response, the kelp production in this region increases by 200 g m^{-2} on average (not shown). However, low DIN concentrations of 1-2 μmol L^{-1} still remain. This indicates that the rapid uptake by kelp exceeds the natural supply in the system, and aquaculture drag further impedes the supply from the Yellow Sea, worsening the limitation in these areas. In the inner bay, the DIN concentration decreases by roughly 1 μmol L^{-1} in case D0 throughout the bivalve monoculture zone and by 3 μmol L^{-1} at the southwestern corner of the bay. This demonstrates that, although the southwestern corner is not directly occupied by aquaculture, the cumulative effects of aquaculture drag on the transport in the bay can significantly increase the nutrient concentration at this location and elevate the risk of eutrophication.

To better understand the effects of aquaculture drag on transport, we time-average the depth-integrated volume fluxes to remove the tides and analyze the residuals. The time-averaging is computed over a fortnight from April 21 to May 8, 2006. Figure 17 shows the spatial distribution of these fluxes (equivalent to volumetric fluxes per unit width) for cases B and D0. The results clearly demonstrate that the residual fluxes are stronger in case D0
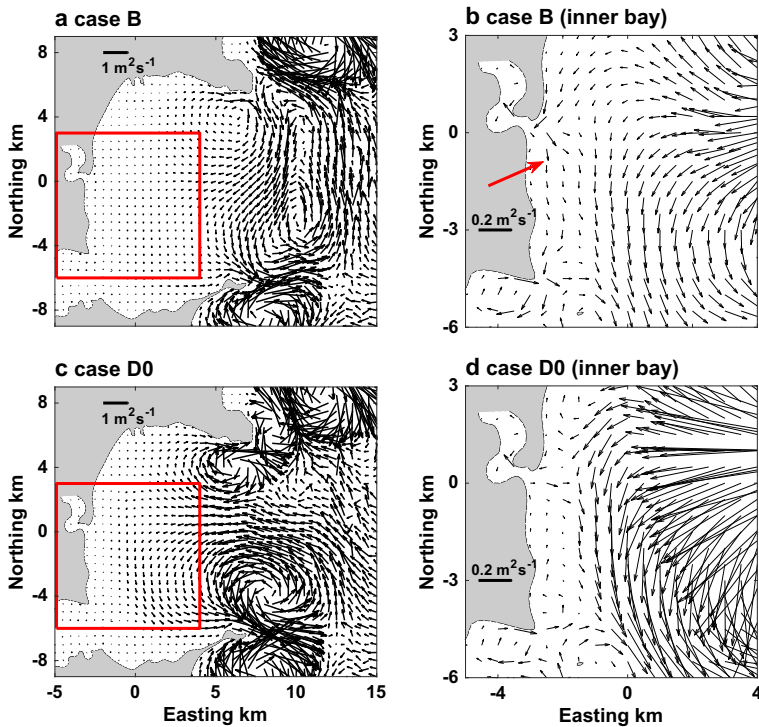

Fig. 17 Predictions of depth-integrated residual fluxes for case B (a, b) and case D0 (c, d). b and d show the regions within the red boxes in a and c. The red arrow in b indicates the southward along-shore flux discussed in the text

than those in case B, and also show considerably different flux patterns. In case D0, two strong recirculation zones are situated near the opening at the northern and southern ends of the bay (Fig. 17c), implying active exchange across the bay opening. In case B, these recirculation zones are substantially weaker. Instead, an elliptical recirculation zone develops along the outer edge of the kelp monoculture zone outside the bay, where the direction of the residual fluxes changes from westward (into the bay) to southward (cross flow parallel to the bay mouth). These findings confirm that the exchange between Sanggou Bay and the Yellow Sea is considerably reduced by the presence of aquaculture drag.

The residual fluxes at the inner bay are also affected by the aquaculture drag, as shown in Fig. 17b, d. In both case B and D0, the residual fluxes decrease from east to west as expected, and the direction of the fluxes is consistent. In the aquaculture zones, residual fluxes are 20%-40% weaker in magnitude in case B than those in case D0. One important feature is that an along-shore southward flux in the inner bay, indicated by the red arrow in Fig. 17b, is more prominent in case B. Most nearshore regions shallower than 5 m are not occupied by aquaculture (see Figs. 2 and 4). In response to the large-scale forcing that drives the north-to-south residual flux through Sanggou Bay, a slightly stronger residual flux is driven along these shallow regions in case B when aquaculture adds additional drag in the deeper regions.

5.2 Impacts of aquaculture on river-borne DIN

River inflow brings high concentrations of nutrients into the bay, and the additional aquaculture drag during the peak kelp growing season can increase the retention along the inner coast and the southwestern region of the bay. We study the transport of river-borne DIN under three scenarios: (1) no aquaculture (case A0), (2) no aquaculture drag (case D0), and (3) the base case (case B). River inflow is assume to be 1 m^3 s^{-1} with a DIN concentration of 100 μmol L^{-1}. Signals due to the river inflow are calculated as the difference in DIN concentrations between the runs with and without the river inflow. Details of the setup are described in Sect. 2.6.
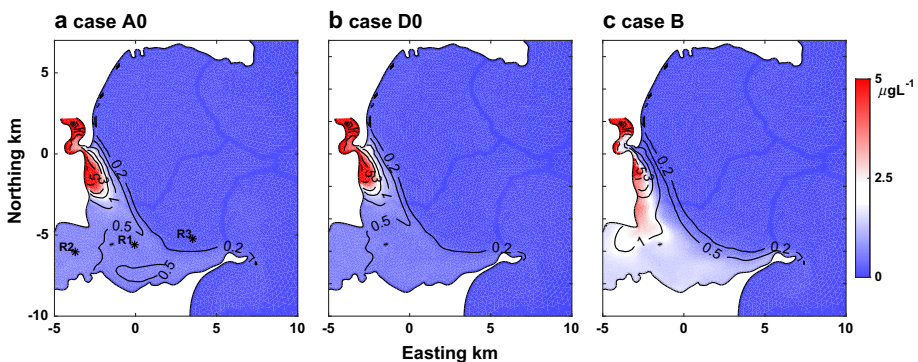

Fig. 18 Model results of river-borne DIN, calculated as differences between the scenarios with and without river inflows for scenario **a** case A0, **b** case D0, and **c** case B. Contours and color schemes are both for river-borne DIN concentrations

As shown in Fig. 18a–c, in general, the area of influence due to river inflow is similar in all three cases. Most of the river load is transported southward along the coastline and flushed out of the bay to the south. Transport to the north is negligible.

In cases A0 and D0, the transport patterns are similar, as illustrated in Fig. 18a, b. The highest concentration occurs within 2 km from and to the south of the river inlet in very shallow regions (less than 3 m deep) with a peak DIN concentration of roughly 6 μmol L^{-1}. At the southwestern corner and the southern part of the bay where the depth is less than 6 m, the river inflow produces a relatively smooth increase of 0–1 μmol L^{-1}. In most of the regions impacted by river-borne DIN, the difference in DIN between case A0 and D0 is only 0.1 μmol L^{-1}. Such a similarity confirms that the DIN load from the river has little interaction with the aquaculture.

In case B, the DIN distribution is considerable altered, as shown in Fig. 18c. First, the high-DIN region formed near the river mouth is less concentrated and more dispersed along the shoreline. This is likely a result of more prominent advective transport to the south along the shore in case B as illustrated by the residual flux in Fig. 17b. Secondly, more DIN retention occurs in the southern and western portions of the bay, with near doubling of the river-borne DIN concentrations in case A0 and D0. This effect can easily be more pronounced under realistic conditions given that we impose a relatively small river flow rate (1/6 of the annual mean) and low DIN concentration (1/3 of the mean). These results indicate that the risk of eutrophication associated with river input is considerably increased during the peak kelp growing season and should be carefully monitored.

For a more quantitative analysis, time series of river-borne DIN concentrations are shown in Fig. 19. Three locations (R1, R2, and R3) within the impacted areas in the southern portion of the bay (see Fig. 18a for the locations) are examined. Location R1 is at the southwestern end of the bivalve cultivation zone. Location R2 is within the southwestern corner (near Bahe Port) where DIN concentrations are usually the highest. Location R3 is within the polyculture zone where the lowest DIN concentrations occur.

For all three cases, the river-borne DIN reaches locations R1 and R2 in roughly 6 days, while a sooner but weaker signal reaches location R3 in 3 days. The tidal fluctuations at location R3 are very strong while the river-borne DIN levels at all three locations fluctuate with the spring-neap cycle and tend to peak during the neap tide. A quasi-periodic equilibrium is reached after roughly two spring-neap cycles. The results from case A0 and D0 are again shown to be similar (Fig. 19). In case B, the river signal is considerably stronger at locations R1 and R2 while weaker at location R3, which is likely caused by less river-borne DIN entering the polyculture zone due to drag. These findings are consistent with the spatial distributions in Fig. 18, and quantitatively show that the aquaculture drag alters the transport of the river-borne DIN and doubles the DIN retention in the southern regions of the bay.

It is worth mentioning that the modeled DIN signals can be linearly extrapolated to estimate results for a range of river flow rates and input DIN concentrations. We have tested up to an annual mean flow rate of 6 m^3 s^{-1}, and the DIN concentrations scale linearly and increase roughly by a factor of 6. The linear scaling occurs because the currents due to river inflow, on the order of 1×10^{-3} m s^{-1} near the river inlet, are much weaker than the tidal flows and thus have a negligible effect on the large-scale circulation. The transport behavior of DIN applies to other passive river-borne substances, such as nutrients and contaminants. For instance, we can expect bioaccumulative contaminants
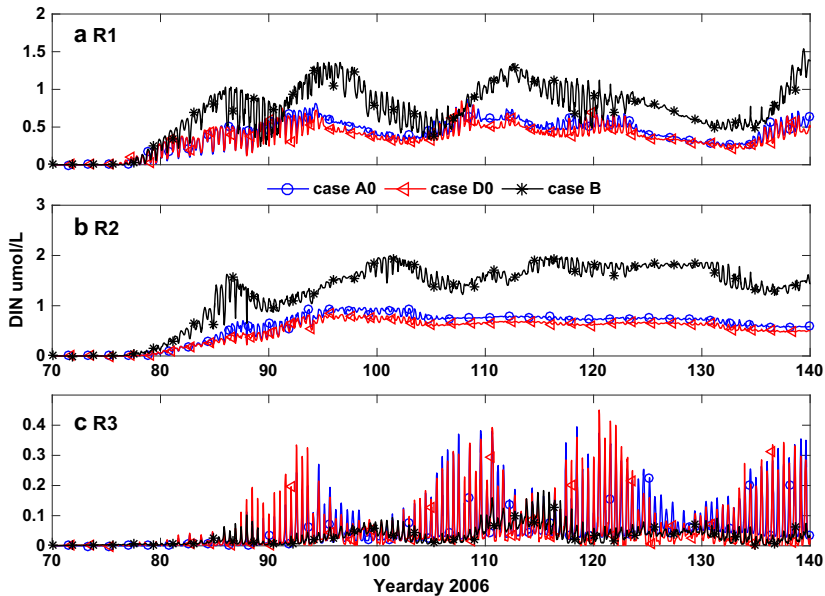
Fig. 19 Time series of river-borne DIN at location **a** R1, **b** R2, and **c** R3 in case A0, D0 and B. Signals are calculated as the differences between cases with and without the river input. Locations R1, R2 and R3 are shown in Fig. 18a

from the river to be mostly uptaken by bivalves cultivated in the shallow southern regions of the bay.

6 Conclusions

In this study, we present a numerical model for Sanggou Bay, one of the largest coastal aquaculture sites in China, to evaluate the influence of intensive aquaculture systems on the hydrodynamics and nutrient transport during the peak kelp growing season. Model validation using publicly available data demonstrates good model accuracy and strong predictive capability. The model predicts the formation of energetic eddies along the irregular coastline of Sanggou Bay that were not resolved by earlier models [11, 24, 44].

Our main findings are: (1) model results indicate strong spatial variability in DIN and a coexistence of DIN depletion and retention as a result of aquaculture; (2) analysis of depth-integrated residual fluxes demonstrates remarkable changes in circulation and reduction in exchange across the bay opening due to the aquaculture drag; and (3) test cases with hypothetical river inflows show that river-borne DIN is mostly transported to the southern regions of the bay and its retention is considerably increased by aquaculture.

These findings, including strong spatial variability, circulation patterns, DIN transport, and kelp production, can be useful in providing a scientific basis for aquacultural and environmental management in Sangou Bay. For example, if fertilizer is applied to improve kelp production as suggested by Zhang et al. [53], the model can readily be used to identify the location and the timing of its application in a way that maximizes the absorption by kelp while minimizes the effects in the inner bay. A similar modeling approach can be

applied to many other aquaculture sites to understand their unique hydrodynamic characteristics and assist with management for long-term sustainability.

References

1. Bleck R (2002) An oceanic general circulation model framed in hybrid isopycnic-cartesian coordinates. Ocean Model 4:55–88
2. Blumberg AF, Mellor GL (1987) A description of a three-dimensional coastal ocean circulation model. In: Heaps N (ed) Three-dimensional coastal ocean models. American geophysical union, Washington, DC, pp 1–16
3. Blumberg AF, Galperin B, O'Connor DJ (1992) Modeling vertical structure of open-channel flows. J Hydraul Eng 118:1119–1134
4. Bolin B, Rodhe H (1973) A note on the concepts of age distribution and transit time in natural reservoirs. Tellus 25(1):58
5. Boller ML, Carrington E (2006) In situ measurements of hydrodynamic forces imposed on chondrus crispus stackhouse. J Exp Mar Biol Ecol 337:159–170
6. Boyd AJ, Heasman KG (1998) Shellfish mariculture in the benguela system: water flow patterns within a mussel farm in Saldanha Bay, South Africa. J Shellfish Res 17:25–32
7. Cao L, Naylor R, Henriksson P, Leadbitter D, Metian M, Troell M, Zhang W (2015) China's aquaculture and the world's wild fisheries. Science 347:133–135
8. Chen C, Liu H, Beardsley RC (2003) An unstructured grid, finite-volume, three-dimensional, primitive equations ocean model:application to coastal ocean model: application to coastal ocean and estuaries. J Atmos Ocean Technol 20:159186
9. Deleersnijder E, Campin JM, Delhez EJM (2001) The concept of age in marine modelling i. Theory and preliminary model results. J Mar Syst 28(3–4):229–267
10. Delhez EJM, Campin JM, Hirst AC, Deleersnijder E (1999) Toward a general theory of the age in ocean modelling. Ocean Model 1(1):17–27
11. Duarte P, Meneses R, Hawkins AJS, Zhu M, Fang J, Grant J (2003) Mathematical modelling to assess the carrying capacity for multi-species culture within coastal waters. Ecol Model 168:109–143
12. Egbert GD, Bennett AF, Foreman MGG (1994) Topex/poseidon tides estimated using a global inverse model. J Phys Oceanogr 15(C12):24821–24852
13. Fan X (2008) Preliminary studies on the features of tidal-dynamic structure in a typically high density mariculture coastal bay-observation and simulations. PhD thesis, Ocean University of China, Qingdao, China, 132 pp
14. Fang J, Zhang J, Xiao T, Huang D, Liu S (2016) Integrated multi-trophic aquaculture (IMTA) in Sanggou Bay, China. Aquac Environ Interact 8:201–205
15. FAO (1989) Culture of Kelp (Laminaria Japonica) in China. Food and Agriculture Organization of the United Nations, RAS/86/034, Training Manual
16. FAO (2014) The state of world fisheries and aquaculture. Food and Agriculture Organization of the United Nations, Rome
17. FAO (2015) FAO global aquaculture production database updated to 2013 summary information. Food and Agriculture Organization of the United Nations, Rome
18. Fenocchi A, Sibilla S (2016) Hydrodynamic modelling and characterisation of a shallow fluvial lake: a study on the superior lake of mantua. J Limnol 75(3):455
19. Fringer OB, Gerritsen M, Street RL (2006) An unstructured-grid, finite-volume, nonhydrostatic, parallel coastal ocean simulator. Ocean Model 14:139–173
20. Fu M, Pu X, Wang Z, Liu X (2013) Integrated assessment of mariculture ecosystem health in sanggou bay. Acta Ecol Sinica 33(1):238–248
21. Gaylord B, Denny MW, Koehl MAR (2008) Flow forces on seaweeds: field evidence for roles of wave impingement and organism inertia. Biol Bull 215:295–308
22. Geider RJ, Roche JL (2002) Redfield revisited: variability of C:N: P in marine microalgae and its biochemical basis. Eur J Phycol 31:1–17

23. Gibbs MM, James MR, Pickmere SE, Woods PH, Shakespear BS, Hickman RW, Illingworth J (1991) Hydrodynamics and water column properties at six stations associated with mussel farming in Pelorus Sound 1984–85. N Z J Mar Freshwater Res 25:239–254

24. Grant J, Bacher C (2001) A numerical model of flow modification induced by suspended aquaculture in a Chinese Bay. Can J Fish Aquat Sci 58:1003–1011

25. Hoffmann MR (2004) Application of a simple space-time averaged porous media model to flow in densely vegetated channels. J Porous Media 7:183–191

26. Jackson GA, Winant CD (1983) Effect of a kelp forest on coastal currents. Cont Shelf Res 2(1):75–80

27. Johnson AS (2001) Drag, drafting, and mechanical interactions in canopies of the red alga chondrus crispus. Biol Bull 201:126–135

28. Kim SJ, Stoesser T (2011) Closure modeling and direct simulation of vegetation drag in flow through emergent vegetation. Water Resour Res 47(10):W10,511

29. Kishi MJ, Uchiyama M, Iwata Y (1994) Numerical simulation model for quantitative management of aquaculture. Ecol Model 79:21–40

30. Li R, Liu S, Zhang J, Jiang Z, Fang J (2016) Sources and export of nutrients associated with integrated multi-trophic aquaculture in Sanggou Bay, China. Aquac Environ Interact 8:285–309

31. Liu H, Qi Z, Zhang J, Mao Y, Fang J (2013) Ecosystem service and value evaluation of different aquaculture mode in Sungo Bay. China Ocean University Press, Qingdao

32. Liu Z (2016) On the eutrophication level of mariculture zone in Sanggou Bay based on fuzzy synthesis evaluation. Ocean Dev Manag 3:43–47

33. Liu Z, Wei H (2007) Estimate of the TKE dissipation and shear stress in the bottom boundary layer in the Yellow Sea. Progress Nat Sci 17(3):362–369

34. Lueck R (2009) Turbulence in the benthic boundary layer. In: Thorpe SA (ed) Encyclopedia of ocean sciences: elements of physical oceanography. Academic Press, Cambridge, pp 311–316

35. MAPRC (2001) Environmental-friendly food technical specifications of laminaria japonica Aresch-Agricultural industry standard of People's Republic of China. NY/T 5057-2001

36. Mellor GL, Oey LY, Ezer T (1998) Sigma coordinate pressure gradient errors and the seamount problem. J Atmos Ocean Technol 35(1):1122–1131

37. Monson N, Cloern J, Lucas L, Monismith S (2002) A comment on the use of flushing time, residence time, and age as transport time scales. Limnol Oceanogr 47(5):1545–1553

38. Nepf HM (1999) Drag, turbulence, and diffusion in flow through emergent vegetation. Water Resour Res 35(2):479–489

39. Nepf HM (2012) Flow and transport in regions with aquatic vegetation. Ann Rev Fluid Mech 44(1):123–142

40. Oldham CE, Sturman JJ (2001) The effect of emergent vegetation on convective flushing in shallow wetlands: scaling and experiments. Limnol Oceanogr 46:1486–1493

41. Rayson M, Gross ES, Monismith SG, Fringer OB (2015) Modelling the tidal and sub-tidal hydrodynamics in a shallow, micro-tidal estuary. Ocean Model 89:29–44. https://doi.org/10.1016/j.ocemod.2015.02.002

42. Rosman JH, Monismith SG, Denney MW, Koseff JR (2010) Currents and turbulence within a kelp forest (macrocystis pyrifera): insights from a dynamically scaled laboratory model. Limnol Oceanogr 55(3):1145–1158

43. Rosmond TE (1992) The design and testing of the navy operational global atmospheric prediction system. Weather Forcast 7:262–272

44. Shi J (2009) Numerical study on the influences of physical processes on the aquaculture carrying capacity in a semi-enclosed bay. PhD thesis, Ocean University of China, Qingdao, China, 126 pp

45. Sun Y, Song Y, Cui Y, Fang J (1996) Distribution and behavior of dissolved inorganic nitrogen in the aquaculture zone in Sanggou Bay China. Mar Fish Res 17(2):52–59

46. Teague WJ, Pistek P, Jacobs GA, Perkins HT (2000) Evaluation of the tides from topex/poseidon in the bohai and yellow seas. J Atmos Ocean Technol 17:679–687

47. Wang B, Zhao G, Fringer OB (2011) Reconstruction of vector fields for semi-Lagrangian advection on unstructured, staggered grids. Ocean Model 40(1):52–71

48. Wood TM (2008) Modeling hydrodynamics and heat transport in upper Klamath Lake, Oregon, and implications for water quality. Technical Report, United States Geological Survey

49. Wu Y, Chaffey J, Law B, Greenberg DA, Drozdowski A, Page F, Haigh S (2014) A three-dimensional hydrodynamic model for aquaculture: a case study in the Bay of Fundy. Aquac Environ Interact 5:235248

50. Yu R, Liu D (2016) Harmful algal blooms in the coastal waters of China: current situation, long-term changes and prevention strategies. J Chin Acad Sci 31(10):11167–11174

51. Zhang J, Jiang Z, Wang W, Zou J, Xue S, Fang J, Lian Y, Zhang X, Liu X, Zhou Y (2010) Seasonal distribution and variation of nutrients and nutrients limitation in Sanggou Bay. Prog Fish Sci 31(4):16–25
52. Zhang J, Wang W, Han T, Liu D, Fang J, Jiang Z, Liu X, Zhang X, Lian Y (2012) The distributions of dissolved nutrients in spring of Sungo Bay and potential reason of outbreak of red tide. J Fish China 36(1):132–139
53. Zhang J, Wang W, Ren JS, Lin F (2016a) A model for the growth of mariculture kelp saccharina japonica in Sanggou Bay, China. Aquac Environ Interact 8:273–283
54. Zhang Z (2010) Numerical simulations of nonlinear internal waves in the South China Sea. Ph.D. thesis, Stanford University, Stanford, California
55. Zhang Z, Lv J, Ye S, Zhu M (2007) Values of marine ecosystem services in Sanggou Bay. Chin J Appl Ecol 18(11):2540–2547
56. Zhang Z, Huang H, Liu Y, Yan L, Bi H (2016b) Effects of suspended culture of the seaweed laminaria japonica aresch on the flow structure and sedimentation process. J Ocean Univ China 15:643–654
57. Zink P (2012) Application of a porous media approach for vegetation flow resistance. In: Mūnoz RM (ed) River flow, proceedings of the international conference on fluvial hydraulics, San Jose, Costa Rica, 5–7 September, 2012, CRC Press, Boca Raton. pp 301–308
58. Zinke P (2010) Flow resistance parameters for natural emergent vegetation derived from a porous media model. In: Dittrich A, Koll K, Aberle J, Geisenhainer P (eds) River flow, proceedings of the international conference on fluvial hydraulics, Braunschweig, Germany, September 08–10, 2010, pp 461–468